Introducing Shape Constraint via Legendre Moments in a Variational Framework for Cardiac Segmentation on non-Contrast CT Images

J. Wojak, Elsa D. Angelini, Isabelle Bloch

INTRODUCING SHAPE CONSTRAINT VIA LEGENDRE MOMENTS IN A VARIATIONAL FRAMEWORK FOR CARDIAC SEGMENTATION ON NON-CONTRAST CT IMAGES

Julien Wojak, Elsa D. Angelini and Isabelle Bloch
Institut Telecom, Télécom ParisTech, CNRS LTCI, 75013 Paris, France
{*julien.wojak, elsa.angelini, isabelle.bloch*}*@telecom-paristech.fr*

Keywords: Segmentation, Medical imaging, Shape constraint.

Abstract: In thoracic radiotherapy, some organs should be considered with care and protected from undesirable radiation. Among these organs, the heart is one of the most critical to protect. Its segmentation from routine CT scans provides valuable information to assess its position and shape. In this paper, we present a novel variational segmentation method for extracting the heart on non-contrast CT images. To handle the low image contrast around the cardiac borders, we propose to integrate shape constraints using Legendre moments and adding an energy term in the functional to be optimized. Results for whole heart segmentation in non-contrast CT images are presented and comparisons are performed with manual segmentations.

1 INTRODUCTION

In thoracic radiotherapy, some organs should be considered with care and protected from undesirable radiation. Among these organs, the heart is one of the most critical in this context. It is therefore useful to have a good knowledge of the heart position and shape, for applications such as dose estimation and therapy planning. This information can be provided by image segmentation. Routine examinations rely on non-contrast CT scans, in which the heart is often difficult to distinguish from surrounding structures based on only grey level information. Manual segmentation is tedious and prone to inter-observer variability, thus calling for automated methods, we which address in this paper.

Among the existing approaches, in (Ecabert et al., 2008) a multi-chamber (i.e. complete heart) mesh model is deformed to segment the heart on high contrast and high resolution CT images. Unfortunately, this method does not apply to non-contrast CT. In (Moreno et al., 2008), the segmentation is constrained using fuzzy representations of anatomical knowledge about the position of the heart in the thorax and with respect to the lungs. This leads to a good robustness but to an average similarity index when compared to manual segmentation of 0.74, which might be too limited for radiotherapy applications.

In this paper, we propose to integrate shape constraints into a variational method,following the idea of (Foulonneau et al., 2006), and based on the model of (Mory and Ardon, 2007). Shape information is represented using Legendre moments and integrated as an additional energy term in the functional to be optimized. Results for whole heart segmentation on non-contrast CT images are presented and evaluated.

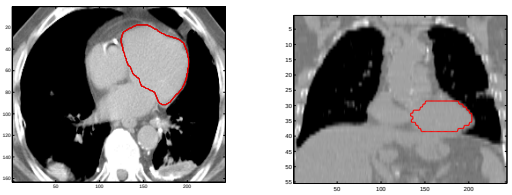

Figure 1: Non-contrast CT thoracic images with manual heart segmentations.

2 VARIATIONAL SEGMENTATION BASED ON GRAY LEVEL INTENSITY

In (Mory and Ardon, 2007), the authors introduced a fuzzy region competition framework to segment an image I into two classes (background and foreground) based on the minimization of the following functional:

$$\min_{u\in BV_{[0,1]}(\Omega)} E_{TV_g}(u(\mathbf{x}),\alpha_i) = \min_{u\in BV_{[0,1]}(\Omega)} \underbrace{\int_\Omega g|\nabla u|\mathrm{d}\Omega}_{\text{regularity}} + \tau\underbrace{\left(\int_\Omega u(\mathbf{x}) r_{\alpha_i}(\mathbf{x})\mathrm{d}\Omega\right)}_{\text{fidelity to the data}} \quad (1)$$

where u is a membership function in $BV_{[0,1]}(\Omega)$ (the space of functions of bounded variations), g is a weighting function of the regularization term in order to relax the regularization near important contours (for example $g = \frac{1}{1+|\nabla \tilde{I}|}$ with $\tilde{I}$ a smooth version of I), and $\mathbf{x}$ denotes the coordinates triplet (x,y,z). The function $r_{\alpha_i}(\mathbf{x})$ (α_i is a set of parameters) could have different expressions such as the well known Chan and Vese region competition term $r_{c_1,c_2}(\mathbf{x}) = (I-c_1)^2 - (I-c_2)^2$ where c_1 and c_2 are the mean intensity in each region (Chan and Vese, 2001), or Paragios and Deriche geodesic active region term $r(\mathbf{x}) = \ln\frac{P(I|\alpha_1)}{P(I|\alpha_2)}$(Paragios and Deriche, 1999). The formulation in Equation 1 leads to several interesting properties:

- using a membership function u instead of a classical indicator function as in (Chan and Vese, 2001) leads to a greater stability of the segmentation process and to a better control of the regularity of the final contours;
- as the space of solutions is the BV space, the membership function u converges toward an indicator function, and therefore a simple thresholding at the end of the minimization process provides the final segmentation;
- as the regularization term is convex, the final result is not sensitive to the initialization.

In this work, we use the region competition approach, with the same formulation as in Equation 1, leading to a fast and flexible segmentation tool to extract the lung cavities and internal blood vessels as illustrated in Figure 2(a-b).

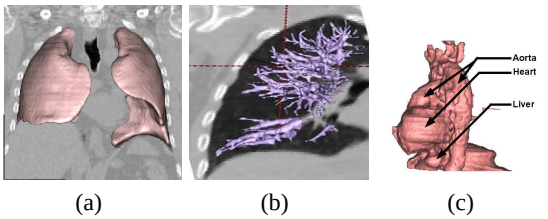

(a) (b) (c)

Figure 2: Segmentation using the region competition formulation: (a-b) lungs and lung vessels (c) the heart is not well separated from the liver and the aorta.

However, since this approach only relies on intensity discrimination into two classes (or phases), it cannot segment different structures having similar gray level characteristics. An example in 2(c) illustrates the difficulty of separating the heart from adjacent structures such as the major blood vessels and the liver, on non-contrast CT data. In order to overcome such limitations, we propose to constrain the segmentation using shape information.

3 SHAPE CONSTRAINT

Several methods have been proposed to constrain shapes in a segmentation functional. In (Gastaud et al., 2004), a distance between a reference and the observed shapes is used. In (Leventon et al., 2000), a PCA analysis is performed on the level sets functions of training segmentations. A review of shape constraints for level sets segmentation methods can be found in (Cremers et al., 2007). For the foreseen applications for thoracic radiotherapy, we have to achieve a compromise between the constraint on the shape characterization and the flexibility of the representation to cope with inter-patient variability (patient positioning, heart size,...). In this context it is not relevant to compute directly a difference between a reference shape and the current shape segmentation. We prefer to control an indirect match by comparing our segmentation with a generic shape model representation that does constrain natural anatomic variability, and is not sensitive to translation and scale variability. Such characteristics can be provided by well-chosen shape moments. For example in (Rose et al., 2009), Tchebichev moments are used to constrain a region growing algorithm, and Foulonneau et al. (Foulonneau et al., 2006) used Legendre moments as shape descriptors in an active contour segmentation framework.Our approach follows a similar scheme as in this last work.

3.1 Legendre Moments

In (Teague, 1980), Teague introduced moments for image analysis. He proposes to use Legendre polynomials or Zernike polynomials as kernel functions. This is motivated by the orthogonality property of both types of polynomials, which guarantees the non-redundancy of the description of an image or a shape. The existence of efficient methods to easily and fastly compute Legendre moments has guided our preference for these moments over Zernike ones. Legendre moments are more sensitive to noise than Zernike moments, but in our framework we manipulate descriptors only on clean binary masks or membership functions defined on $[0,1]$, in a framework of fuzzy

region competition. Therefore this limitation is not a drawback for the proposed approach.

Legendre moments are defined by the projection of a function on a polynomial basis. Let $I : [-1,1]^3 \rightarrow \mathbb{R}$ be the image representation. The moment of I of order $p+q+r$ is defined as:

$$\lambda_{pqr} = C_{pqr} \int_{[-1,1]^3} P_p(x)P_q(y)P_r(z)I(x,y,z)dxdydz \quad (2)$$

where $C_{pqr} = \frac{(2p+1)(2q+1)(2r+1)}{8}$ and P_p,P_q,P_r are Legendre polynomials, defined by the following two order recursive relation:

$$P_{p+1}(x) = \frac{2p+1}{p+1}xP_p(x) - \frac{p}{p+1}P_{p-1}(x) \quad (3)$$

($p > 1$, $P_0(x) = 1$ and $P_1(x) = x$).
Legendre polynomials form an orthogonal basis, with:

$$\frac{2p+1}{2}\int_{-1}^{1} P_p(x)P_q(x)dx = \begin{cases} 0 & \text{if } p \neq q \\ 1 & \text{if } p = q \end{cases} \quad (4)$$

Working with a finite number of moments, an estimate $\hat{I}$ of I is given by:

$$\hat{I}(x,y,z) = \sum_{p=0}^{L}\sum_{q=0}^{p}\sum_{r=0}^{q} \lambda_{p-q,q-r,r}P_{p-q}(x)P_{q-r}(y)P_r(z) \quad (5)$$

where L is the maximum order for which Legendre moments are computed.

The computation can be performed with the fast and exact Hosny method (Hosny, 2007). First, the spatial image domain is embedded in the cube $U = [-1,1]^3$. Assuming that the image has $X \times Y \times Z$ voxels, the centers of voxels are then given by the coordinates (x_i, y_j, z_k) such that

$$\begin{array}{l} x_i = -1 + (i-1/2)\Delta x \;\; i = 1 \cdots X \quad \text{and } \Delta x = \frac{2}{X} \\ y_j = -1 + (j-1/2)\Delta y \;\; j = 1 \cdots Y \quad \text{and } \Delta y = \frac{2}{Y} \\ z_k = -1 + (k-1/2)\Delta z \;\; k = 1 \cdots Z \quad \text{and } \Delta z = \frac{2}{Z} \end{array} \quad (6)$$

Voxels on wich the image intensity is constant are then defined as intervals $[U_i, U_{i+1}] \times [V_j, V_{j+1}] \times [W_k, W_{k+1}]$ with

$$\begin{array}{ll} U_i = x_i - \Delta_x/2 & U_{i+1} = x_i + \Delta_x/2 \\ V_j = y_j - \Delta_y/2 & V_{j+1} = y_j + \Delta_y/2 \\ W_k = z_k - \Delta_z/2 & W_{k+1} = z_k + \Delta_z/2 \end{array} \quad (7)$$

The moment expression computed on the whole image can then be rewritten as:

$$\lambda_{p,q,r} = C_{p,q,r}\sum_{i=1}^{L}\sum_{j=1}^{M}\sum_{k=1}^{N} I(x_i,y_j,z_k)\int_{U_i}^{U_{i+1}}\int_{V_j}^{V_{j+1}}\int_{W_k}^{W_{k+1}} P_p(x)P_q(y)P_r(z)\mathrm{d}x\mathrm{d}y\mathrm{d}z \quad (8)$$

Moreover thanks to the following recursive primitive property of the Legendre polynomes

$$\int_{cst}^{x} P_p(y)dy = \frac{P_{p+1}(x) - P_{p-1}(x)}{2p+1}, \quad (9)$$

Legendre moments can be written as:

$$\lambda_{pqr} = \sum_{i=1}^{L}\sum_{j=1}^{M}\sum_{k=1}^{N} I_p(x_i)I_q(y_j)I_r(z_k)I(x_i,y_j,z_k) \quad (10)$$

where $I_p(x_i) = \frac{2p+1}{2p+2}\left[xP_p(x) - P_{p-1}(x)\right]_{U_i}^{U_i+1}$ and similar expressions for I_q and I_r. The kernel $I_pI_qI_r$ is independent of the image intensity and can therefore be precomputed. Moreover the separability property allows us to compute the 3D moments using three 1D steps.

To guarantee scale and translation invariances, Legendre moments must be reformulated in the following way:

$$\Lambda_{pqr} = C_{pqr}\int_{[-1,1]^3} P_p(\tfrac{x-x_0}{\mathcal{A}})P_q(\tfrac{y-y0}{\mathcal{A}})P_r(\tfrac{z-z_0}{\mathcal{A}})I(x,y,z)dxdydz \quad (11)$$

where (x_0, y_0, z_0) are the coordinates of the center of inertia of I and $\mathcal{A}$ is the volume of the shape.

3.2 Discriminating Volumes by a Finite Number of Legendre Moments

Two similar shapes have the same set of Legendre moments and two different shapes have two different sets of Legendre moments. However, since we work with scale and translation invariant moments, the set $\{\lambda_{0,0,0}, \lambda_{0,0,1}, \lambda_{0,1,0}, \lambda_{1,0,0}\}$ is the same for each shape and should not be used for discriminating between shapes. In order to illustrate the discriminative power of the moments, we consider four classes of shapes: *class 1:* heart alone, *class 2:* heart and aorta together, *class 3:* heart and liver together, *class 4:* heart and liver and aorta together.

Norm 2 Error. To highlight differences between Legendre moments of the four classes of shapes, we compute the square ℓ_2 norm between two shapes as $||\lambda_{\text{shape}_1} - \lambda_{\text{shape}_2}||_2^2$ where λ_{shape_i} is a vector storing successive Legendre moments of a shape. Comparing the measures for a finite number of moments from a mask of a reference heart and objects for the other classes we obtain the following results (Table 1):

Errors at order 5 are inferior to those at order 15. This is due to the fact that small order moments represent low frequency shape information. The gap between moment differneces between hearts and between hearts and other structures is more important for order 5 (factor 5) than for order 15 (factor 2). It is due to the fact that at order 5, the difference between

Table 1: ℓ_2 norm of the difference between sets of Legendre moments between a reference heart shape and 13 maks of others hearts, 4 masks of hearts and liver, 4 masks of hearts and aorta, 4 masks of hearts and aorta and liver.

	mean		min		max	
order / ref vs	5	15	5	15	5	15
other hearts	0.17	1.21	0.13	1.09	0.26	1.52
heart and liver	0.56	2.40	0.52	2.26	0.58	2.56
heart and aorta	0.61	2.38	0.44	2.13	0.69	2.50
heart and aorta and liver	0.53	2.38	0.45	2.19	0.62	2.60

(a) (b) (c) (d) (e)

Figure 3: Examples of mask of: (a) reference heart, (b-c) two other hearts, (d) heart and aorta, (e) heart and liver.

shapes of different classes is sufficiently important to discriminate between them, and in the same class differences of the shape are too small to well discriminate between them.
In the following experiment we compare moments at a maximum order 10 in order to well differentiate shapes and to take advantage of the global representation of a shape by its moments.

PCA Analysis. In this section, we study the capability of Legendre moments to efficiently discriminate between correctly segmented hearts and erroneous segmentations, by considering again the four classes of shapes. Inspired by (Poupon et al., 1998), we performed a PCA analysis on a matrix in which each raw is an observation, i.e. a segmentation result, and each column corresponds to an ordered list of Legendre moments. The PCA analysis shows that the first three modes represent 90% of the variance. As illustrated in Figure 4, the moments also discriminate efficiently the different types of shapes. Indeed samples from the heart alone are well grouped in the plane of the first two modes and are well separated from the other types of shapes.

3.3 Introducing Shape Constraint in the Functional

We propose to introduce an additional term in the segmentation functional to be optimized through a comparison between moments of a reference shape and moments of the current segmented shape, as follows:

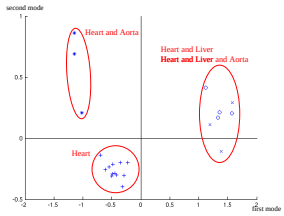

Figure 4: PCA on Legendre moments. Result on the first two principal axes, "+" heart alone, "o" heart and liver, "*" heart and aorta, "x" heart and liver and aorta.

$$\min_{u\in BV([0,1])} \int_\Omega g|\nabla u|\mathrm{d}\Omega + \tau\int_\Omega r(\mathbf{x})u\mathrm{d}\Omega + \frac{\gamma}{2}||\lambda^{\mathrm{ref}} - \lambda^{\mathrm{cur}}(u)||_2^2 \tag{12}$$

This formulation is quite similar to the one described in (Foulonneau et al., 2006). However, using a membership function u instead of a level set function leads to a more stable algorithm. Another difference concerns the order of the used moments. Since one of the main objectives of the work by (Foulonneau et al., 2006) was to provide an algorithm robust to occlusions, a hard constraint on the shape was needed and high order moments were computed. In our framework, the goal is to capture global features of the shape and allow a small variability between them. Therefore only quite small order moments are needed.

Minimization. We perform the minimization of the functional (12) by a gradient descent method.
To insure that $u \in BV_{[0,1]}(\Omega)$ in (1) we rewrite it in the same manner as in (Chan et al., 2005) :

$$\min_u E_{TV_g}(u(\mathbf{x})) = \min_u \int_\Omega g|\nabla u|\mathrm{d}\Omega + \tau\left(\int_\Omega u(\mathbf{x})r(\mathbf{x})\mathrm{d}\Omega\right) + \int_\Omega \alpha\nu_\varepsilon(u)\mathrm{d}\Omega + \frac{\gamma}{2}||\lambda^{\mathrm{ref}} - \lambda^{\mathrm{cur}}(u)||_2^2 \tag{13}$$

where ν_ε is a regularized approximation of the penality function $\nu(a) = \max\{0, 2|a-1/2|-1\}$ with $\alpha > ||r(\mathbf{x})+||\,||\lambda^{\mathrm{ref}} - \lambda^{\mathrm{cur}}(u)||_2^2||_\infty$
and we obtain the following iterative scheme:

$$u^{(n+1)}(\mathbf{x}) = u^n(\mathbf{x}) + dt\left[\mathrm{div}(g\frac{\nabla u(\mathbf{x})}{|\nabla u(\mathbf{x})|}) - \tau r(\mathbf{x}) - \alpha\nu'_\varepsilon(u) - \gamma\sum_{p,q,r}\left((\lambda^{\mathrm{ref}}_{p,q,r} - \lambda^{\mathrm{cur}}_{p,q,r}(u))P_p(x)P_q(y)P_r(z)\right)\right]$$

Choise of r. Let us arbitrarily define the heart region as the foreground region, (i.e. the region in which we would like to obtain $u(\mathbf{x}) = 1$) and the rest of the region of interest as the background region (i.e. the region in which we would like to obtain $u(\mathbf{x}) = 0$).
Histograms of the foreground and the background

intensities,obtained from manual segmentations, are shown in Figure 5. It shows that intensities values are quite similar in the background and in the foreground. However, the intensity is very homogeneous in the heart and presents two peaks in the background.

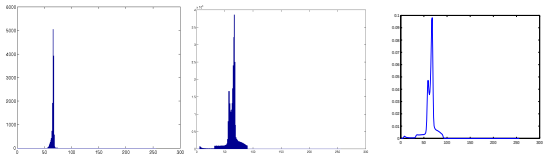

Figure 5: Histograms of foreground (left) and background (middle) intensities. Right: background intensity probability density estimation using Parzen window.

We use this difference to construct the following relevant data fidelity term $r(\mathbf{x})$:

$$r(\mathbf{x}) = (I-c_1)^2 - (\max((I-c_1)^2))(\int_{\mathcal{B}}(p(b)-K(I-b))^2 db \qquad (14)$$

where $c_1 = \frac{\int_\Omega I(\mathbf{x})u(\mathbf{x})d\mathbf{x}}{\int_\Omega u(\mathbf{x})d\mathbf{x}}$ is the empirical estimation mean of the heart intensity, $\mathcal{B}$ is the interval of the image intensities, p is the Parzen estimation of the probability density function of the intensity of the background, expressed as:

$$p(b) = \frac{1}{||1-u||_1}\int_\Omega (1-u(\mathbf{x}))K((I(\mathbf{x})-b)/\sigma)d\mathbf{x} \qquad (15)$$

where K is a Gaussian window ($K(a) = \frac{1}{\sqrt{2\pi}}\exp(-\frac{a^2}{2})$) and σ is chosen sufficiently small to distinguish the two modes in the background area.

Choice of τ and γ. CT images are calibrated, whith known tissue intensity values (for examples compact bones are known to be around 1000 Hounsfield units (HU)). This intensity inter-images stability calibration allows us to pre-set the weight of each term in the functional in order to insure a good balance between them. The regularization term, computed on manual segmentations, is of the order of 10^6 (it corresponds to the surface of the whole heart weighted by g). The data fidelity term is close to zero. The shape constraint term at order 10 falls within the range of values $[1,2]$. Finally, by dividing g by 10^6 a good balance between all terms in the functional (12) is obtained for τ and γ in $]0,\ 10[$. We performed several experiments for different parameters and finally we fixed $\tau = 1.4$ and $\gamma = 0.8$ for all tests summarized in Table 2.

Table 2: Quantitative results: comparison between automatic and manual segmentations. The numbers in parentheses are results obtained by (Moreno et al., 2008).

	similarity index	sensitivity	specificity
Heart 1	0.82 (0.77)	0.96 (0.96)	0.74 (0.64)
Heart 2	0.81 (0.70)	0.89 (0.90)	0.78 (0.58)
Heart 3	0.80 (0.75)	0.94 (0.78)	0.70 (0.72)
Heart 4	0.84 (0.74)	0.76 (0.62)	0.97 (0.92)
Heart 5	0.77 (0.84)	0.81 (0.83)	0.72 (0.84)
Heart 6	0.81 (0.80)	0.93 (0.91)	0.71 (0.71)
Heart 7	0.78 (0.71)	0.84 (0.88)	0.73 (0.60)
Heart 8	0.80 (0.67)	0.92 (0.71)	0.80 (0.62)
Heart 9	0.75 (0.64)	0.83 (0.60)	0.73 (0.70)

4 HEART SEGMENTATION

Masking a Region of Interest and Initializing. From a pre-segmentation of the lungs, a region of interest (ROI) around the heart is built as the bounding box of lungs elongated at the bottom to insure that the heart is completely inside. A mask of the lungs and the trachea is removed from the ROI.

(a) (b) (c)

Figure 6: Preprocessing. (a) Heart ROI with lungs and trachea masked out. (b) Example of an initialization of the hear segmentation. (c) Gradient weighting function g around the heart.

Moreover tissues at the right of the left lung and at the left of the right lung are removed. This is illustrated in Figure 6.
The initialization is performed semi-automatically. A point C approximatively at the center of the heart is marked and the initial value of $u(\mathbf{x})$ is defined by $u(\mathbf{x}) = 1$ if $\mathbf{x}$ is both inside a sphere centered at C with 4 cm diameter and inside the region of interest, and $u(\mathbf{x}) = 0$ otherwise.

Tests and Results. Tests on 9 non contrast CT scan have been performed. For each one, the result of the segmentation was compared with a manual delineation done by an expert. Similarity, sensitivity and specificity indices are computed and reported in Table 2. We also compared our results with those obtained by the method of Moreno (Moreno et al., 2008). We globally obtain better results than those obtained by Moreno et al. Differences between the results of the two methods are illustrated in Figures 7(b) and 8. Ex-

cept for the heart 4 (Figure 8 column 2), the specificity index is generally higher than the sensitivity. It means that our automatic segmentation often provides a larger region than the manual one (it is mainly due to the fact that a small part of the aorta is often included in the segmentation of the heart, as illustrated in Figure 7(a).

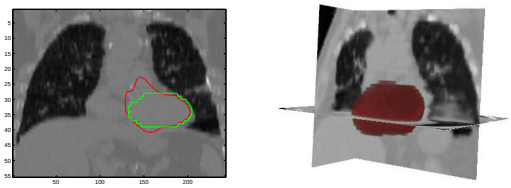

(a) (b)

Figure 7: (a) Automatic segmentation (in red) includes small part of the aorta (green: manual segmentation). (b) A 3D view of a whole heart segmentation.

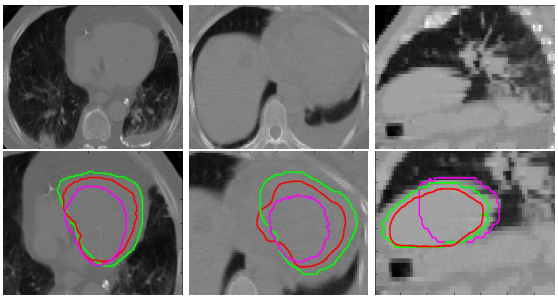

Figure 8: Examples of segmentation results. First row: original image, second row: image superimposed with segmentations (green expert segmentation, magenta Moreno et al segmentation, red our automatic segmentation).

5 CONCLUSIONS

We have adapted a fuzzy region competion framework for the segmentation of the heart in non-contrast CT images by adding a shape constraint. Shape informations was encoded with Legendre moments. Since we work with CT images (which are calibrated), we use hard a priori on the image intensity. The initialization is performed semi-automatically using a spherical approximation of the heart. Several tests on clincal cases provide satisfying results. In particular, the shape constraint allows us to achieve a good separation between the heart and surrounding organs (liver, aorta), improving the initial fuzzy region competition model. When compared to another method (Moreno et al., 2008) using structural knowledge (but no shape information) the results are also improved. This framework could be extended in a sequential way to segment other organs in the thorax like the aorta.

ACKNOWLEDGEMENTS

This work was partially funded by the Medicen Pôle de Compétitivité within the Miniara project.

REFERENCES

Chan, T. F., Esedoglu, S., and Nikolova, M. (2005). Finding the global minimum for binary image restoration. In *ICIP*, pages I: 121–124.

Chan, T. F. and Vese, L. A. (2001). Active contours without edges. *IEEE Trans. Image Processing*, 10(2):266–277.

Cremers, D., Rousson, M., and Deriche, R. (2007). A review of statistical approaches to level set segmentation: Integrating color, texture, motion and shape. *International Journal of Computer Vision*, 72(2):195–215.

Ecabert, O., Peters, J., and etal (2008). Automatic model-based segmentation of the heart in CT images. *IEEE Trans. Medical Imaging*, 27(9):1189–1201.

Foulonneau, A., Charbonnier, P., and Heitz, F. (2006). Affine-invariant geometric shape priors for region-based active contours. *IEEE Trans. Pattern Analysis and Machine Intelligence*, 28(8):1352–1357.

Gastaud, M., Barlaud, M., and Aubert, G. (2004). Combining shape prior and statistical features for active contour segmentation. *IEEE Trans. Circuits and Systems for Video Technology*, 14(5):726–734.

Hosny, K. M. (2007). Exact Legendre moment computation for gray level images. *Pattern Recognition*, 40(12):3597–3605.

Leventon, M. E., Grimson, W. E. L., and Faugeras, O. D. (2000). Statistical shape influence in geodesic active contours. In *CVPR*, pages I: 316–323.

Moreno, A., Takemura, C. M., Colliot, O., Camara, O., and Bloch, I. (2008). Using anatomical knowledge expressed as fuzzy constraints to segment the heart in CT images. *Pattern Recognition*, 41(8):2525–2540.

Mory, B. and Ardon, R. (2007). Fuzzy region competition: A convex two-phase segmentation framework. In *Scale Space and Variational Methods in Computer Vision*, pages 214–226.

Paragios, N. and Deriche, R. (1999). Geodesic active contours for supervised texture segmentation. In *CVPR*, pages II: 422–427.

Poupon, F., Mangin, J. F., Hasboun, D., Poupon, C., and Magnin, I. (1998). Multi-object deformable templates dedicated to the segmentation of brain deep structures. In *Medical Image Computing and Computer-Assisted Intervention - MICCAI 1998*, pages 187–196.

Rose, J.-L., Revol-Muller, C., Charpigny, D., and Odet, C. (2009). Shape prior criterion based on Tchebichef moments in variational region growing. In *ICIP*.

Teague, M. R. (1980). Image analysis via the general theory of moments. *Journal of the Optical Society of America*, 70(8):920–930.